

# Predicting DOC Concentration in the Peel River with a Mechanistic Numerical Model

MSc Thesis

Erik Young (Utrecht University)

Supervisors

Dr. Lubos Polerecky (Utrecht University)

Dr. Jorien Vonk (Vrije Universiteit Amsterdam)

Niek Speetjens, M.Sc. (Vrije Universiteit Amsterdam)

Utrecht University

May 23, 2021

## Abstract

Arctic warming is causing increased export of sediments and organic matter via active layer deepening and thermokarst slumps. A mechanistic numerical model was developed using the **ReacTran R** package to predict riverine dissolved organic carbon (DOC) and total suspended sediment (TSS) concentrations measured during a 2019 field expedition in the Peel River watershed, YT, Canada. In addition to advective transport, two geochemical DOC removal processes were implemented (DOC mineralization and adsorption to mineral surfaces). The power of upstream slump affected area to predict riverine DOC and TSS concentrations was also investigated via a random forest classifier used to identify slump features in the landscape. However, other landscape properties (NDVI, NDMI) proved to be better predictors of riverine DOC and TSS, possibly due to inaccuracies in the classification. Steady state model results indicate that 70–90 % of total DOC input to the river was exported from the downstream boundary unaffected by removal processes, and the 10–30 % of input DOC that was removed was done so predominantly via adsorption to mineral surfaces. Adsorption was driven by high TSS tributaries entering the model domain in its downstream reaches, with the high TSS values possibly due to increased slumping activity in the watersheds of these tributaries. Requisite sensitivity analyses were not performed and offer opportunities for continuation of this work, as does expanding the model to include dynamic inputs and splitting the bulk DOM pool into contributing components.

## Acknowledgements

This study was only possible due to the planning and support of the people involved. Jorien Vonk and Niek Speetjens planned and executed an ambitious sampling expedition which provided the data for this project as well as offered their expansive expertise in Arctic carbon dynamics. Lubos Polerecky brought the aquatic systems modeling expertise and an intricate knowledge of the R package used to create this model. He also provided excellent  $\text{\LaTeX}$  support and rapid, thoughtful feedback during the writing process. Ingmar Nitze made the slump classification possible by providing the visualized Landsat 8 trend images and offering his Google Earth Engine expertise, as well as some of the preliminary hydrological analysis. Ignacio Farías Gutiérrez’s geohydrology prowess provided elegantly simple solutions to seemingly unsolvable problems encountered while constraining the input data. Nataliya Issayeva provided exceptional coding assistance, even with applications far outside her day to day work, due to her rock-solid conceptual knowledge of computer science. Anne, Jim, Krista, and Valerie Young provided unwavering support throughout the process. Thank You!

# Contents

<b>1</b>	<b>Introduction</b>	<b>3</b>
<b>2</b>	<b>Methods</b>	<b>4</b>
2.1	Model Framework . . . . .	4
2.2	Preliminary Data Processing . . . . .	6
2.2.1	Predicting Discharge . . . . .	6
2.2.2	Slump and Burn Scar Classification . . . . .	6
2.2.3	Predicting Unmeasured Lateral TSS and DOC . . . . .	7
2.2.4	Cell Volume Estimates . . . . .	7
2.2.5	TSS Correction and Conversion . . . . .	7
<b>3</b>	<b>Results</b>	<b>8</b>
3.1	Preliminary Data Processing . . . . .	8
3.1.1	Predicting Discharge . . . . .	8
3.1.2	Slump and Burn Scar Classification . . . . .	8
3.1.3	Predicting Unmeasured Lateral TSS and DOC . . . . .	9
3.2	Reaction Transport Model Results . . . . .	9
3.2.1	Unmodified Inputs . . . . .	9
3.2.2	Modified Inputs . . . . .	10
3.2.3	State Variable Budgets and Cell Residence Time . . . . .	11
<b>4</b>	<b>Discussion</b>	<b>20</b>
4.1	Slump and Burn Scar Classification . . . . .	20
4.2	Flow Predictions . . . . .	21
4.3	State Variable Concentration Predictions . . . . .	21
4.4	Model Scenarios — Varying rate constants . . . . .	21
4.5	Model Scenarios — Varying Input Fluxes . . . . .	22
4.6	Additional Uncertainty and Limitations . . . . .	22
4.7	Outlook . . . . .	23
<b>5</b>	<b>Conclusions</b>	<b>24</b>

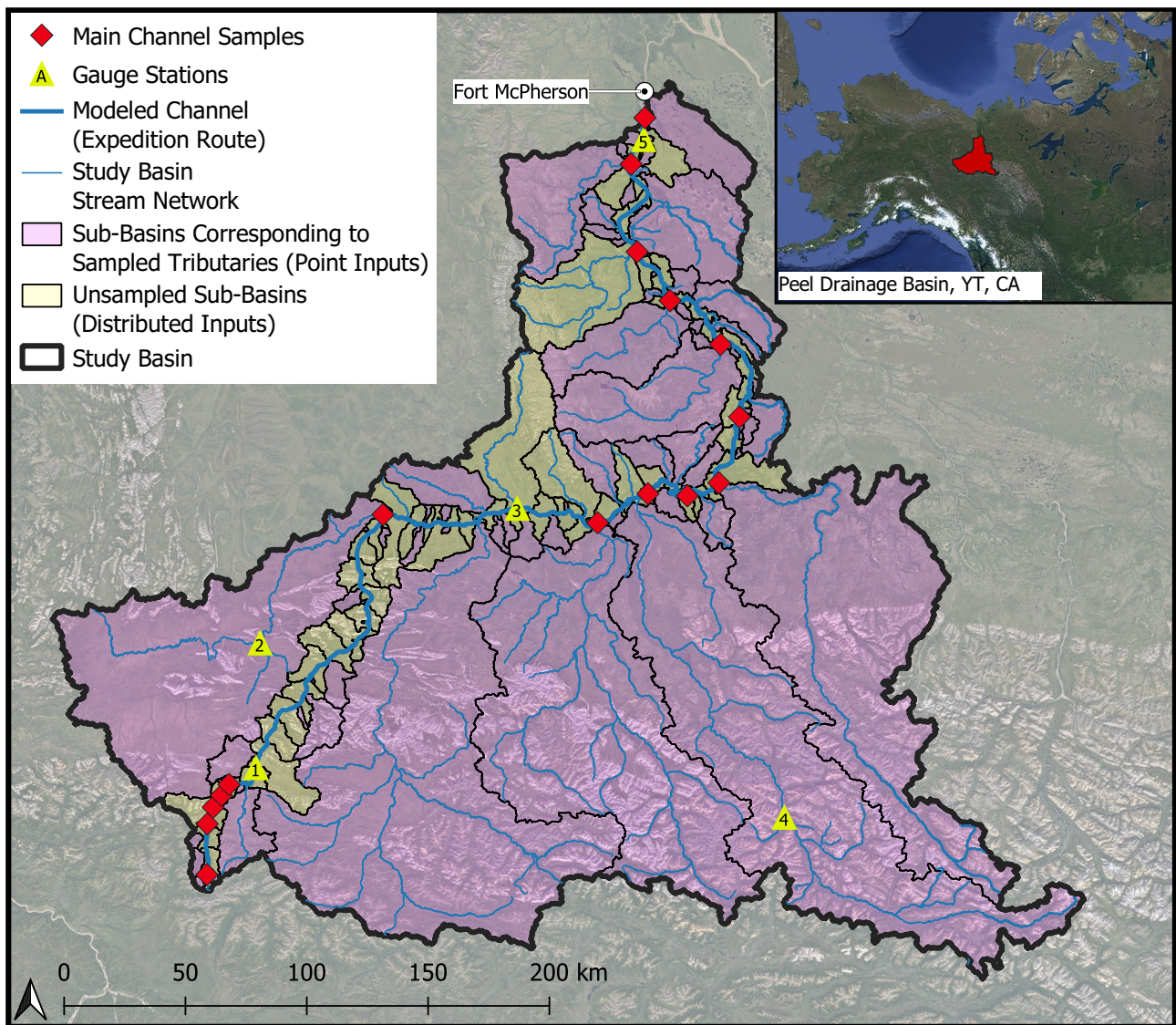


Figure 1: Overview map of the study area with important features.

## 1 Introduction

Arctic warming is causing increased mobilization of dissolved organic matter (DOM) stored in permafrost via active layer deepening. When it occurs in ice-rich permafrost, active layer deepening can cause the soil to collapse into the volume previously occupied by ice (thermokarst). Thermokarst slumps often promote increased erosion and localized thawing via their alteration of landscape morphology. Thermokarst features often fill with water or drain to streams, so they can cause a dramatic export of old organic matter to the stream networks that drain them (Mann et al., 2015; Schuur et al., 2015). While this export is dominated by sediments and particulate organic matter, the DOM fraction is important since its size allows for consumption by bacteria, leading to more rapid degradation of the DOM fraction than its particulate counterpart. The lateral transport and fate of permafrost-sourced DOM is not well described, due in part to spatial variability and complex interactions between the ecosystem characteristics that govern it (Mann et al., 2015; O’Donnell et al., 2016). Local heterogeneities in landscape slope, soil grain size and ice content, and plant population, for example, can be difficult to account for at larger scales but can exert strong controls on riverine DOM concentrations. Another strong

control on permafrost sourced DOM concentrations in the stream network is the preferential consumption by bacteria of said DOM over contemporary DOM (Mann et al., 2015). In some watersheds, this can mean that the older, permafrost-sourced DOM signal could be lost before reaching higher order streams. However, this old DOM remains an important source of carbon that should be included in carbon budgets.

The Peel watershed is a relatively well-studied watershed of 70 680 km<sup>2</sup> in the Yukon and Northwest Territories, Canada. It is underlain by continuous and discontinuous permafrost, with areas of ice-rich permafrost exhibiting dramatic landscape changes (Kokelj et al., 2017). In July and August 2019, a sampling expedition was undertaken as part of the EU Horizon2020 project Nunataryuk, which studies the interactions between people and changes to permafrost with a focus on the Arctic coastal region. This expedition sampled the main stem of the Peel River and its tributaries as it runs north to the Mackenzie river delta. In addition to field measurements of standard water quality parameters, water samples were collected for laboratory analyses of stable isotopes, total suspended sediments (TSS), chromophoric DOM (CDOM), fluorescent DOM (fDOM), dissolved organic carbon (DOC), dissolved inorganic carbon (DIC), and major ions. DOC and TSS measurements were used here.

The objective of this project was to construct a one-dimensional reactive-transport model that can predict DOC concentration in the sampled section of the Peel River, using the expedition data and remote sensing products as inputs. To accomplish this goal, unsampled lateral fluxes of water and solutes into the model domain needed to be estimated. It was hypothesized that upstream slump affected area would be predictive of riverine DOC and TSS concentrations. To test this, upstream slump affected area was calculated via a random forest classifier trained on a composite landscape trend image. The calculated area and six other remote sensed landscape properties were tested for correlation with DOC and TSS concentrations in the river. Once assembled, the input data, in conjunction with the model, provides valuable insights into the processes controlling DOC concentration in the Peel River as well as estimates of carbon removal fluxes by geochemical processes.

## 2 Methods

### 2.1 Model Framework

Reaction transport modeling was performed in one dimension using the `ReacTran R` package (Soetaert and Meysman, 2012; R Core Team, 2017), which is developed for constructing models that numerically solve the advection-dispersion equation (ADE) in 1, 2, or 3 dimensions in porous media or surface waters. The 635.6 km model domain was divided into 5000 equal cells 127.12 m in length (Figure 2a). Data from the sampling expedition was combined with remote sensing products and data from in-situ stream-flow loggers to constrain the lateral and upstream water, DOC, and TSS fluxes into the model domain and estimate the volume of each cell.

Two geochemical processes were implemented: mineralization (referred to as degradation in this text) and adsorption of organic matter (Figure 2b). Degradation was modeled as a first order kinetic process with respect to DOC concentration (i.e., the rate was calculated as  $k_{deg} \times [\text{DOC}]$ , where  $k_{deg}$  is the rate constant ( $\text{d}^{-1}$ ) (Figure 10). Adsorption was also modeled as

an irreversible first order process with respect to DOC and FSS (see [Section 2.2.5](#) for definition of FSS) concentration (i.e., the rate was calculated as  $k_{ads} \times [\text{DOC}] \times [\text{FSS}]$ , where  $k_{ads}$  is the rate constant ( $\text{m}^3 \text{mmol}^{-1} \text{d}^{-1}$ ) ([Figure 10](#)), this formulation assumed that the availability of adsorption sites on the FSS particles was far from the adsorption capacity), due to the lack of data required to model it as an equilibrium process (equilibrium adsorption capacity).

Lateral input fluxes were split into point (sampled tributaries) and diffuse (unsampled zones) sources. Point source fluxes were estimated by providing a predicted discharge for each tributary along with the measured concentrations. Diffuse input fluxes were estimated by dividing the model domain into 50 zones (100 model cells each) and delineating nested watersheds for these zones, from which measured tributary watersheds were subtracted. Predicted discharge and state variable contributions for each resulting zone were calculated from the respective regressions ([Section 2.2.3](#)) and divided equally among the 100 model cells making up each zone. In cells receiving both point and diffuse inputs, the input concentrations were calculated via the following equation:

$$C_{in} = \frac{C_{point} \cdot Q_{point} + C_{diffuse} \cdot Q_{diffuse}}{Q_{point} + Q_{diffuse}}, \quad (1)$$

where  $Q$  refers to discharge and  $C$  refers to concentration. A constant flux upstream boundary condition was implemented via predicted discharge and measured DOC and TSS concentrations at the upstream boundary.

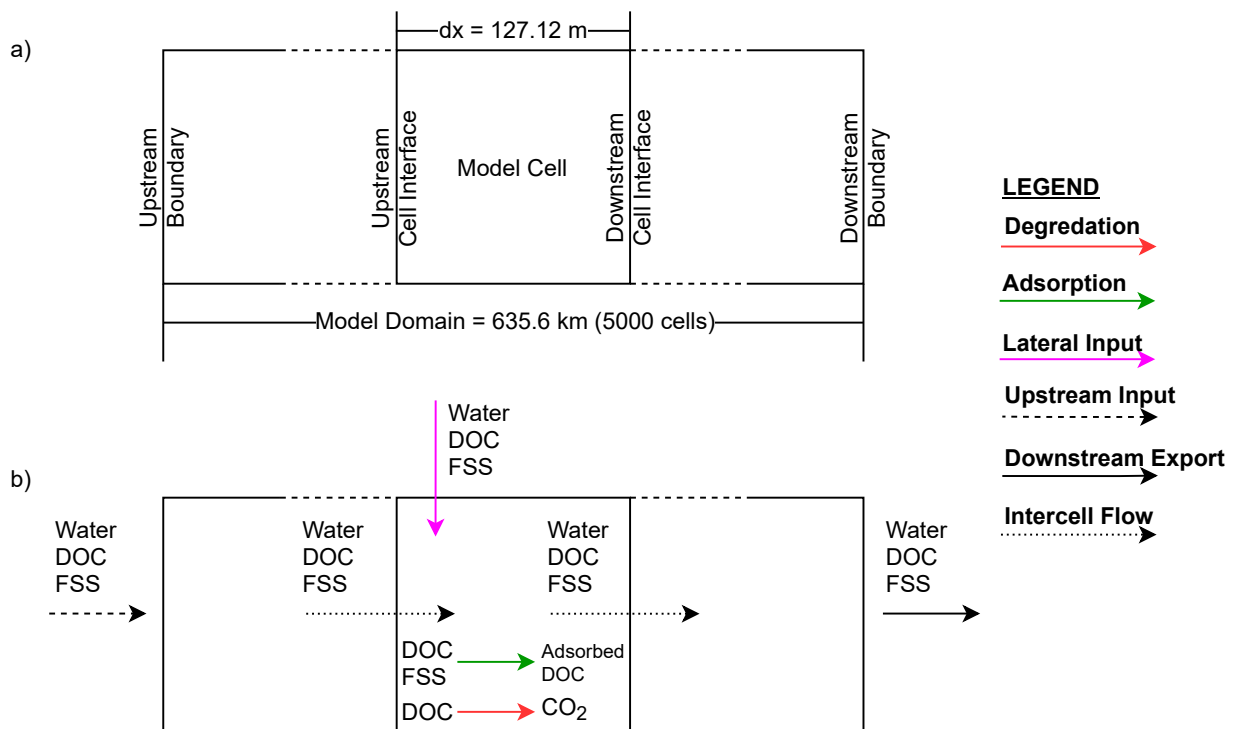


**Figure 2:** (a) Overview of model set up and definition of terminology, and (b) schematic diagram of fluxes considered in the model. Note that the colored arrows in (b) occur in all model cells but are only shown for one model cell here. Lateral inputs consist of point and diffuse sources.

## 2.2 Preliminary Data Processing

Preliminary data processing can be divided into four goals: predicting discharge in the sample basin, predicting lateral DOC and TSS inputs between measured tributaries, estimating the volume of each model cell, and TSS measurement correction and conversion. The first step in achieving the first three goals was a hydrological analysis to facilitate watershed delineation and upstream area calculations. Flow direction and accumulation raster images were created from a 30 m resolution, hydrologically conditioned, digital elevation model (DEM: [Natural Resources Canada, Canadian Digital Elevation Model](#); hydrologic conditioning: Ingmar Nitze, AWI, Potsdam, DE). Since these maps represent a simplification of the landscape, tributary and main channel samples were manually relocated from their real coordinates to their representative channels on the flow accumulation map to enable watershed delineations and upstream area calculations based on these points. Hydrological analyses were performed in TauDEM ([Tarboton, 1997](#)), GRASS GIS ([GRASS Development Team, 2017](#)), and QGIS ([QGIS Development Team, 2021](#)).

### 2.2.1 Predicting Discharge

Discharge predictions at model boundaries and cell interfaces ([Figure 2](#)) were necessary in order to convert input concentrations to mass fluxes and estimate the volume of each model cell. Predicting discharge in the sample basin was accomplished by plotting daily average discharges from five in-situ gauges within the basin ([Natural Resources Canada, Water Level and Flow](#)) over the 32-day sampling period against the upstream area of the gauging location to obtain a linear discharge-area relationship. This regression was used to calculate discharge at any location in the study basin as necessary.

### 2.2.2 Slump and Burn Scar Classification

Although the sampling expedition was extensive, it did not seek to constrain all lateral inputs to the model domain and focused on tributary inputs, so it was necessary to predict lateral DOC and TSS inputs to the model domain in the reaches between sampled tributaries. It was initially hypothesized that the fraction of a measurement's upstream area affected by thermokarst slumping would be a good predictor of riverine DOC and TSS concentrations. In order to estimate the slump affected upstream area fraction, supervised random forest classifiers were trained in Google Earth Engine ([Gorelick et al., 2017](#)) for two (slump, not slump) and three (slump, burn scar, neither) classes from a composite image consisting of 12 bands: 19 year (2000–2019) linear regression slope for normalized difference vegetation and moisture indexes (NDVI, NDMI), tasseled cap brightness, greenness, and wetness (TCB, TCG, TCW), 19 year mean for the same five indices, landscape slope, and landscape elevation (landscape index bands generated from Landsat 8 imagery and provided by Ingmar Nitze, AWI Potsdam, DE). Training data for the slump (143 points), not slump (1087 points), and neither (737 points) classes was created via manual inspection of satellite imagery and landscape index trend imagery, and burn class training data (341 points) was created by randomly sampling from a map of wildfires in the area from 2000–2019 ([Natural Resources Canada, CWFIS Datamart](#)).

### 2.2.3 Predicting Unmeasured Lateral TSS and DOC

Slump affected area was calculated from the classification in [Section 2.2.2](#) for the watershed of each sample location, and tested for correlation against DOC and TSS measurements. Average upstream 19-year mean for the five landscape indices used in the classification ([Section 2.2.2](#)) and average upstream slope were also tested for correlation against riverine DOC and TSS concentrations. Linear regressions were obtained and best predictors of DOC and TSS were selected based on their coefficients of determination.

### 2.2.4 Cell Volume Estimates

The volume of each model cell was required so that the solute transport function could convert between mass and concentration as necessary. Water depth was multiplied by channel width and cell length to produce cell volume. Water depth estimates were made via the assumption that the model domain is a rectangular river much wider than it is deep. This allows the approximation of hydraulic radius by water depth in Manning's Equation ([Manning, 1891](#)), which enables the calculation of water depth ( $h$ , [m]) from discharge ( $Q$ , [ $\text{m}^3 \text{s}^{-1}$ ]), hydraulic head gradient ( $s$ , [-]), width ( $w$ , [m]) and a roughness coefficient ( $n$ , [ $\text{s m}^{-1/3}$ ]):

$$h = w^{-3/5} \cdot Q^{3/5} \cdot s^{-3/10} \cdot n^{3/5}. \quad (2)$$

Hydraulic head gradient ( $s$ ) was assumed to be equal to channel bed slope and was obtained at each model cell interface from a linear piecewise fit of the channel elevation profile ([Figure 11b](#)). Discharge ( $Q$ ) was predicted at each model cell interface via the discharge-area linear regression ([Section 2.2.1](#)). Width ( $w$ ) estimates were obtained by linearly interpolating between 108 manual width estimates made from satellite imagery near the measured tributaries. Other methods to approximate channel width ([Yamazaki et al., 2014](#); [Yang et al., 2020](#)) were explored but ultimately abandoned due to the time required to obtain use-able estimates. A constant roughness coefficient ( $n$ ) estimate of  $0.025 \text{ s m}^{-1/3}$  was applied across the model domain. The chosen value represents a base  $n$  value for a stable channel in firm soil ([Arcement and Schneider, 1989](#), p. 4) and was selected via speculation about the average roughness of the model domain. Proper calculation of the roughness coefficient entails dividing the river into reaches that can be represented by a single roughness value and then calculating the coefficient based on qualitative and quantitative descriptions of channel morphology. While discussion with the field team may have provided at least qualitative descriptions of channel morphology upon which to base a more robust  $n$  calculation, this was not pursued due to time constraints.

### 2.2.5 TSS Correction and Conversion

TSS measurements contained negative values up to  $-2.12 \text{ mg L}^{-1}$  due to filter loss during the measurement process. In the absence of a reliable method to correct for this,  $2.12 \text{ mg L}^{-1}$  TSS was added to all measurements (see [Section 4.6](#) for discussion of this approach). Additionally, the corrected TSS concentrations were converted to a concentration of free adsorption surface sites (FSS) via the following equation:

$$FSS = TSS \cdot SA \cdot (\text{max OC load} - \text{input OC load}), \quad (3)$$

where  $SA$  is the average surface area of suspended sediments ( $27 \text{ m}^2 \text{ g}^{-1}$ ; Bröder et al., 2021),  $max \text{ OC load}$  is the maximum density of organic carbons that can adsorb to a particle ( $0.167 \text{ mmol C m}^{-2}$ ; Bröder et al., 2021) and  $input \text{ OC load}$  is the observed density of organic carbons already adsorbed when the suspended sediments reach the channel ( $0.058 \text{ mmol m}^{-2}$ ; Bröder et al., 2021). This was done to conceptually simplify the modeling of adsorption as a first order, irreversible process (Section 2.1).

## 3 Results

### 3.1 Preliminary Data Processing

#### 3.1.1 Predicting Discharge

The correlation between upstream area and discharge measured at the five gauge stations (station locations: Figure 1) was highly significant ( $p < 0.001$ ; Figure 3). The upstream area described 89 % of the variation in the discharge (Figure 3), which was considered sufficient for the use upstream area as a predictor of discharge at model cell interfaces (Section 2.2.4) and discharge contributions from tributaries and unsampled areas. Areas used for the regression ranged from  $1227.5$  to  $70\,397.5 \text{ km}^2$ , while the areas used to predict discharge ranged from  $0.04$  to  $71\,559.5 \text{ km}^2$ , so it was assumed that areas below  $1227.5 \text{ km}^2$  follow the same relationship to discharge as the areas used in the regression. The remaining 11 % of the variance unexplained by the upstream area was likely due to precipitation. This could not be constrained from available data, but the effect of precipitation can be seen in Figure 3 as the spread of the measured data points for each station over 32 days.

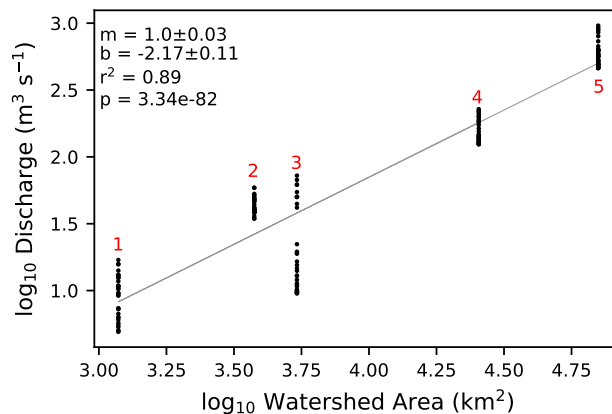


**Figure 3:** 32 daily discharge measurements at five stream-gauge locations in the study basin. Best estimates and standard errors of the slope ( $m$ ) and intercept ( $b$ ) of the linear regression model are shown. Red numbers refer to the locations of the stream gauges marked in Figure 1.

#### 3.1.2 Slump and Burn Scar Classification

The two-class classifier often mis-classified known burn scars as slumps, so the addition of the third class was necessary to separate these features. The three-class classifier predicted a slump affected area of  $286.1 \text{ km}^2$  (0.40 % of the total basin) and a burned area of  $5683.2 \text{ km}^2$  (7.9 %

of the total basin) (Figure 4a, Figure 5a). The total area of the 2000–2019 wildfire data-set from which the training points were sampled is 3066.8 km<sup>2</sup>, but the classifier predicted a burned area 1.9 times this value. Of the 143 slump training points, 135 were correctly classified, three were classified as burn scars, and five were classified as neither slump nor burn scar, indicating an accuracy of 94.4% when compared to the training data. For the burn class, 14 of the 341 training points were classified as neither slump nor burn scar, and none were classified as slump, indicating an accuracy of 95.9% when compared to the training data. 85.6% of the total area of the 2000–2019 wildfire data-set was correctly identified as a burn scar, while 13.7% and 0.7% were classified as neither and slump, respectively. The Google Earth Engine random forest classifier has a built in accuracy metric that describes the probability of each classification being correct. However, this is only implemented for use with two-class classifiers. Manual generation of this metric was predicted to be too time consuming for this project, so no further error metrics are presented for the slump and burn scar classifications.

Qualitative assessment of the slump classification at locations where slump features are obvious from satellite imagery and the landscape trend image reveals that it was able to identify slump features, but often not completely (e.g., Figure 4b,c,d). Many small groups of pixels were identified as slumps but were not clearly identifiable as slumps from satellite imagery and the landscape trend image (e.g., Figure 4b,c,d, top right corner). The burn scar classification exhibits largely the same behavior — most known burn scars were identified, and outside these features the classification takes a more dispersed form (e.g., Figure 5b,c,d). However, the burn classification did identify some larger continuous areas outside of the known burn scars, which may be scars from older burns not contained in the wildfires data set.

### 3.1.3 Predicting Unmeasured Lateral TSS and DOC

DOC and TSS were significantly correlated with all tested indices ( $p < 0.001$ , Figure 6, Figure S1). However, the variance in DOC and TSS explained by the different indices was generally low (DOC: 11–48%, TSS: 0–26%), indicating that most of the observed variance was due to untested sources (precipitation, for example), or perhaps that a multi-variable approach is necessary when attempting to predict DOC and TSS from landscape properties. In the absence of other, more reliable predictors, NDVI and NDMI were selected for DOC and TSS predictions. They described 48% and 26% of the variation in DOC and TSS measurements, respectively (Figure 6d,e).

## 3.2 Reaction Transport Model Results

### 3.2.1 Unmodified Inputs

Steady state model solutions were obtained with unmodified lateral input fluxes and varying reaction rate constants (Figure 7). When judging the quality of fit, priority was given to the DOC predictions, since accurately predicting TSS (via FSS) concentrations was not the focus. Quality of fit was judged visually since extra analysis is necessary to indicate which parameters should be used in a mathematical fitting.

Initially, it was observed that the addition of reactions had the greatest affect on the trend of the DOC profile at a distance of greater than approximately 350 km. With adsorption turned

off, a degradation rate constant of  $0.15 \text{ d}^{-1}$  was required to begin to match the trend in the latter half of the model domain, and had a noticeable effect when compared to the no reactions line starting at a distance of approximately 50 km (Figure 7a, orange line). A degradation rate constant of  $0.15 \text{ d}^{-1}$  corresponds to a half-life of 4.62 days, which was deemed unreasonably short (Catalán et al., 2016). A value of  $0.003 \text{ d}^{-1}$  ( $t_{1/2} = 231 \text{ d}$ ) was selected for the lateral input scenarios as a reasonable DOC degradation constant for terrestrial systems (Catalán et al., 2016). With degradation turned off, an adsorption constant of  $0.0007 \text{ m}^3 \text{ mmol}^{-1} \text{ d}^{-1}$  also began to match the trend in the latter quarter of the river but displayed a vertical offset of roughly  $50 \text{ mmol m}^{-3}$  (Figure 7a). Neither of the rate constant scenarios were able to predict the two DOC peaks at distances of approximately 75 and 375 km in the observed data. Cumulative model flow at the downstream boundary was 81.8% of the average of the 32 daily discharge measurements at the nearby stream-gauge, but was within the range these measurements (Figure 7c).

### 3.2.2 Modified Inputs

Lateral input fluxes of DOC and TSS were manipulated to explore whether model predictions could be made to better fit the measured data (Figure 8). For input scenario 1, lateral input DOC concentration was set to zero between distances of roughly 360 and 400 m (Figure 8b, orange line), and lateral input discharge in this zone was multiplied by 20 (Figure 8a, orange line). The lateral input modifications in scenario 1 successfully offset the latter half of the DOC profile to better match the observed data, and offered minor improvements in the latter half of the FSS profile (Figure 9a,b; orange line). Scenario 1 cumulative model flow at the downstream boundary was 99.7% of the average of the 32 daily discharge measurements at the nearby stream-gauge (Figure 9c, orange line).

Input scenario 2 was created via a more aggressive manipulation of input fluxes in an attempt to match the model output to the observed DOC peaks at roughly 75 and 375 km. Concentration increases were forced by increasing lateral DOC input in targeted zones (Figure 8b, blue line). Setting lateral DOC input to zero was not enough to force a concentration decrease of the required magnitude in most cases, so lateral input flow was also increased in these zones to provide a dilution effect and drive a concentration decrease (Figure 8a, blue line). Input scenario 2 provided a large improvement in the fit of the DOC profile because it was able to predict the measured DOC concentration peaks at approximately 75 and 375 km (Figure 9a). The FSS profile exhibited further improvements over scenario 1 starting at distances greater than 350 km, but showed a greater deviation from the measurements in the first 75 km of the model domain. Cumulative model flow for scenario 2 at the downstream boundary was 180.7% of the average of the 32 daily discharge measurements at the nearby stream-gauge, and 115.8% greater than the maximum daily discharge from the 32 day period (Figure 9c).

Lateral FSS input concentrations were not modified directly in either input scenario, but the lateral input flux of FSS (mass per time) was affected by the input flow modifications (Figure 8c), since the mass flux is equal to the flow times concentration.

### 3.2.3 State Variable Budgets and Cell Residence Time

Under the base input scenario, approximately 72% of total DOC input was exported at the downstream boundary of the model domain, and this value increased to 78% and 90% as flow was added in the two scenarios (Figure 10). Adsorption was responsible for removing approximately 26% (base), 21% (scenario 1), 9.7% (scenario 2) of total input DOC, while degradation only removed approximately 0.73% (base), 0.62% (scenario 1), 0.44% (scenario 2) of total input DOC (Figure 10). Of the total input FSS, approximately 16% (base), 12% (scenario 1), 7.6% (scenario 2) was removed by adsorption, and the remaining 84% (base), 88% (scenario 1), 92% (scenario 2) was transported downstream unaffected by adsorption (Figure 10).

The effect of the input flow modifications on the residence time of water in each model cell and the total model domain was also investigated. Model cell residence time was calculated as cell length (127.12 m) divided by average velocity through each cell, which was calculated by dividing average discharge through each cell by the average cross sectional area of each cell's upstream and downstream interfaces. Residence times ranged from approximately 13 seconds to 4 minutes (Table 1), with zones of high residence time corresponding to flatter areas in the elevation profile (Figure 11). In the base input scenario, the total residence time of water in the model domain was 3.84 days. For input scenarios 1 and 2, the total residence times were 3.51 days and 2.94 days, respectively (Table 1). This corresponds to approximately 8.6% and 35% reductions in total river water residence time for the respective scenarios versus the base scenario.

Input Scenario	Water Residence Time Per Cell (minutes)				
	Mean	Std Dev	Min	Max	Sum
Base	1.11	0.66	0.53	4.09	5533.23
Scenario 1	1.01	0.64	0.43	4.09	5059.86
Scenario 2	0.72	0.45	0.22	2.22	3592.74

**Table 1:** Descriptive statistics for water residence time per cell in the three input scenarios. Residence time was calculated as cell length (127.12 m) divided by average velocity through each cell.

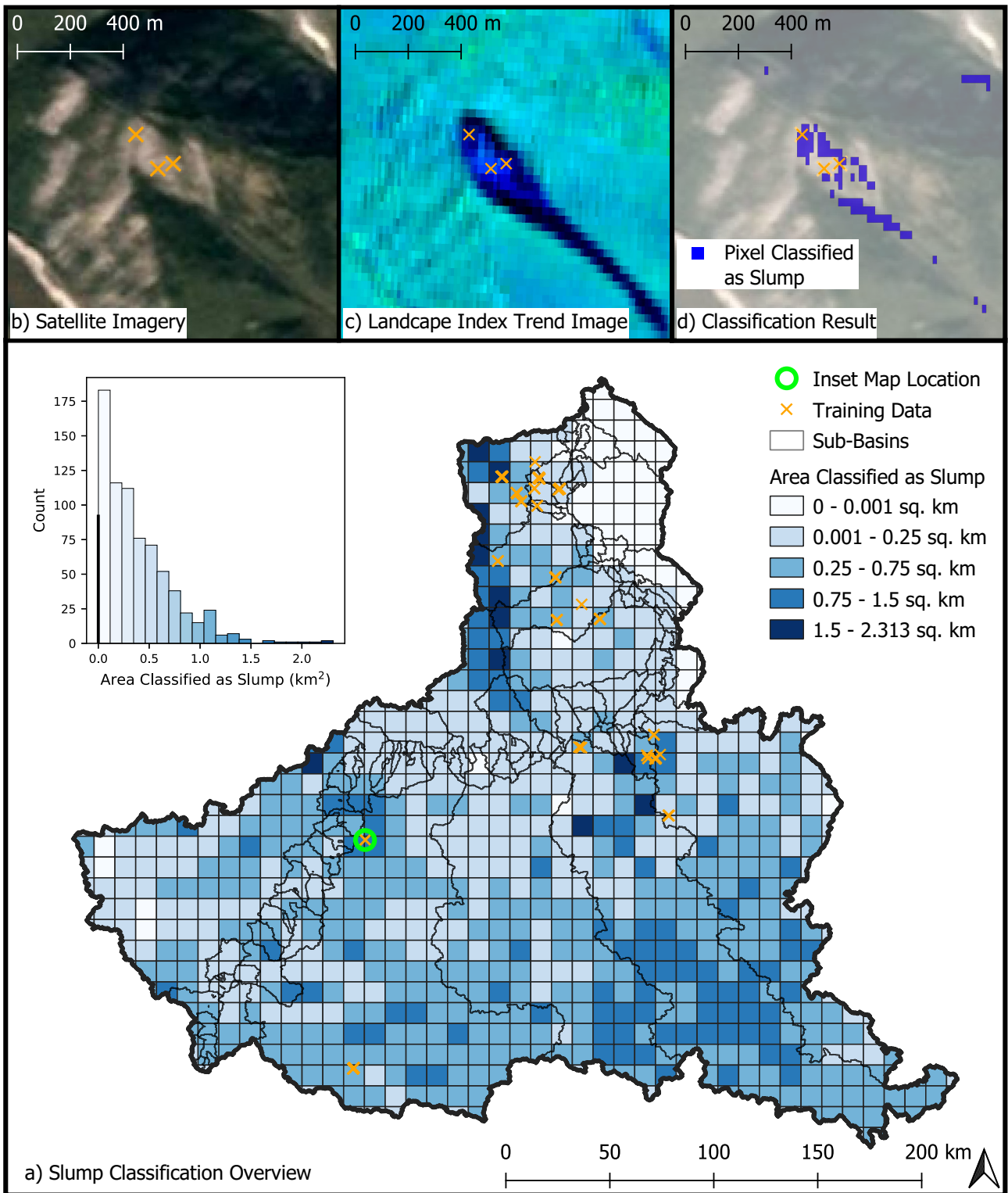


**Figure 4:** Visualizations of the slump classified areas. (a) The study basin is divided into 10 km × 10 km squares which are colored by the area classified as slump within each square. Inset maps show (b) an example slump in satellite imagery, (c) the landscape index trend image used for the classification, and (d) the result of the classification. Note that the inset maps (b,c,d) are smaller (roughly 1.5 km × 1.5 km) than the squares in the overview map (a) due to the scale required to show slump features clearly. The thick black vertical line in the histogram is the first bin (0 to 0.001 km<sup>2</sup>).

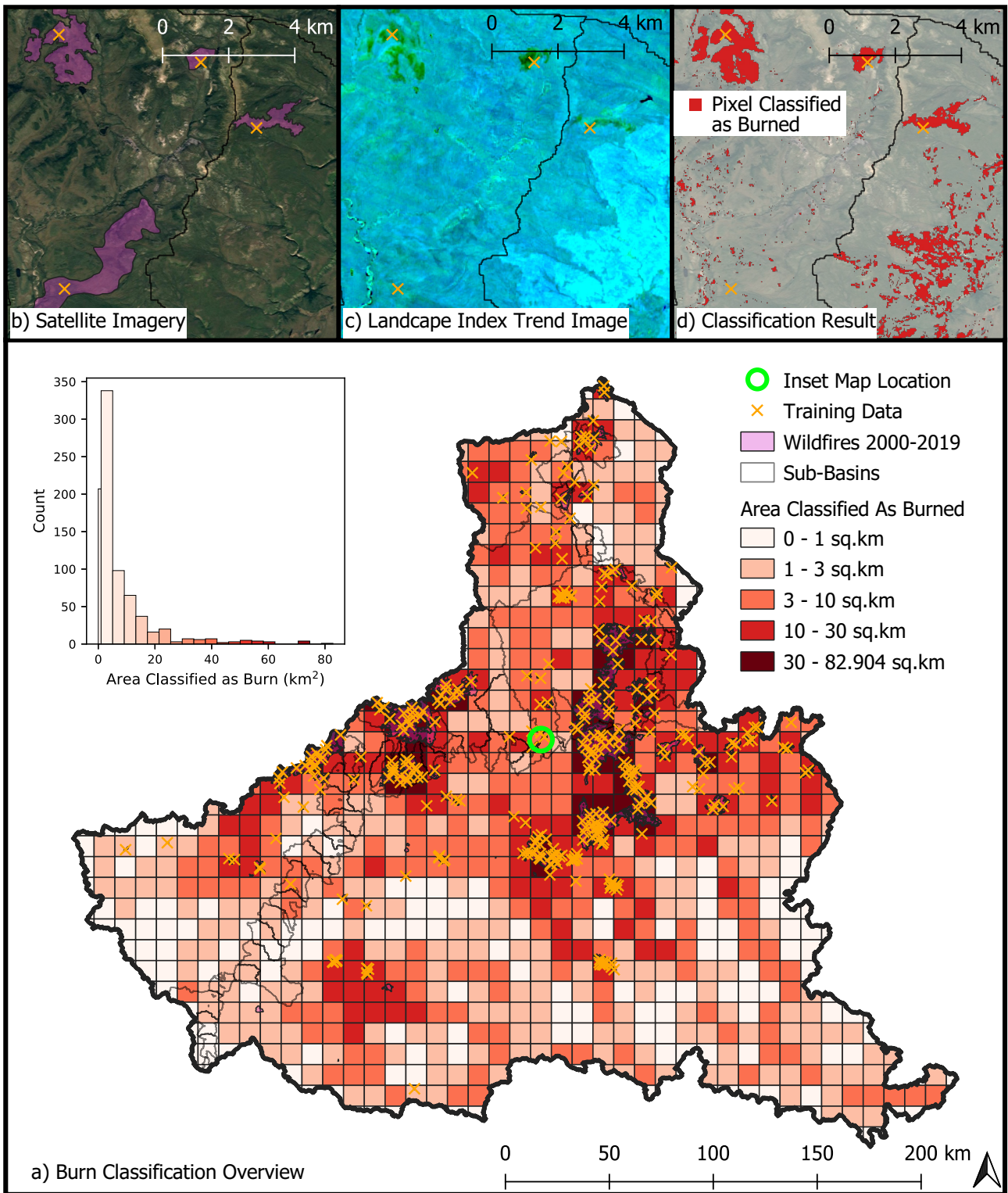


**Figure 5:** Visualizations of the burn scar classified areas. (a) The model domain is divided into  $10\text{ km} \times 10\text{ km}$  squares which are colored by the area classified as a burn scar within each square. Inset maps show (b) an example burn scars in satellite imagery, (c) the landscape index trend image used for the classification, (d) and the result of the classification. Here the inset maps (b,c,d) are showing the extent of one square in the overview map (a). The narrow first bin in the histogram is same as the first category in the map legend (0 to  $1\text{ km}^2$ ).

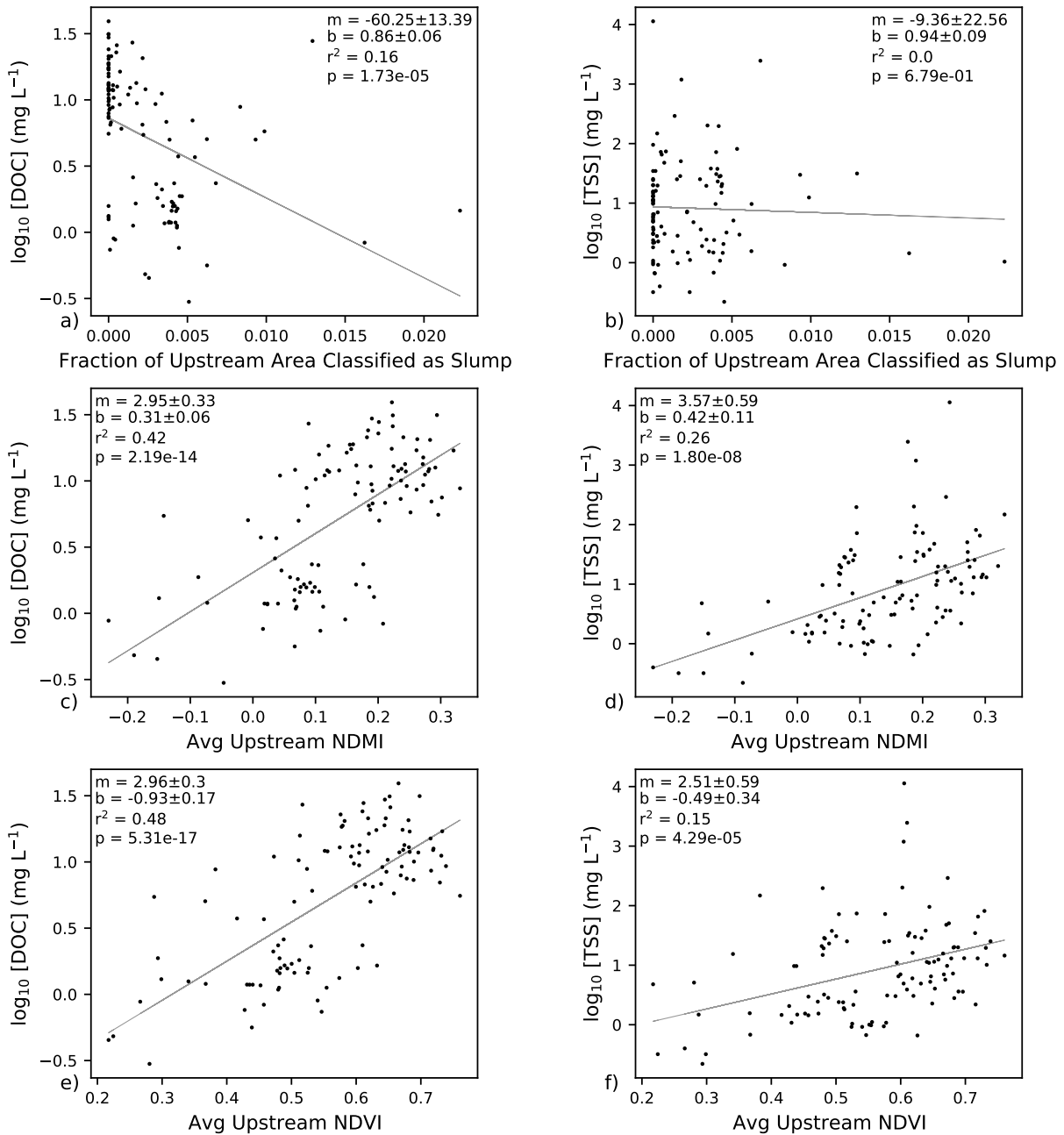


**Figure 6:** DOC (left column) and TSS (right column) measurements tested for correlation against three landscape properties derived from remote sensing products. (e) NDVI and (d) NDMI were chosen to predict DOC and TSS, respectively. See [Figure S1](#) for the remaining four tested landscape properties. Best estimates and standard errors of the slope (m) and intercept (b) of the linear regressions are shown.

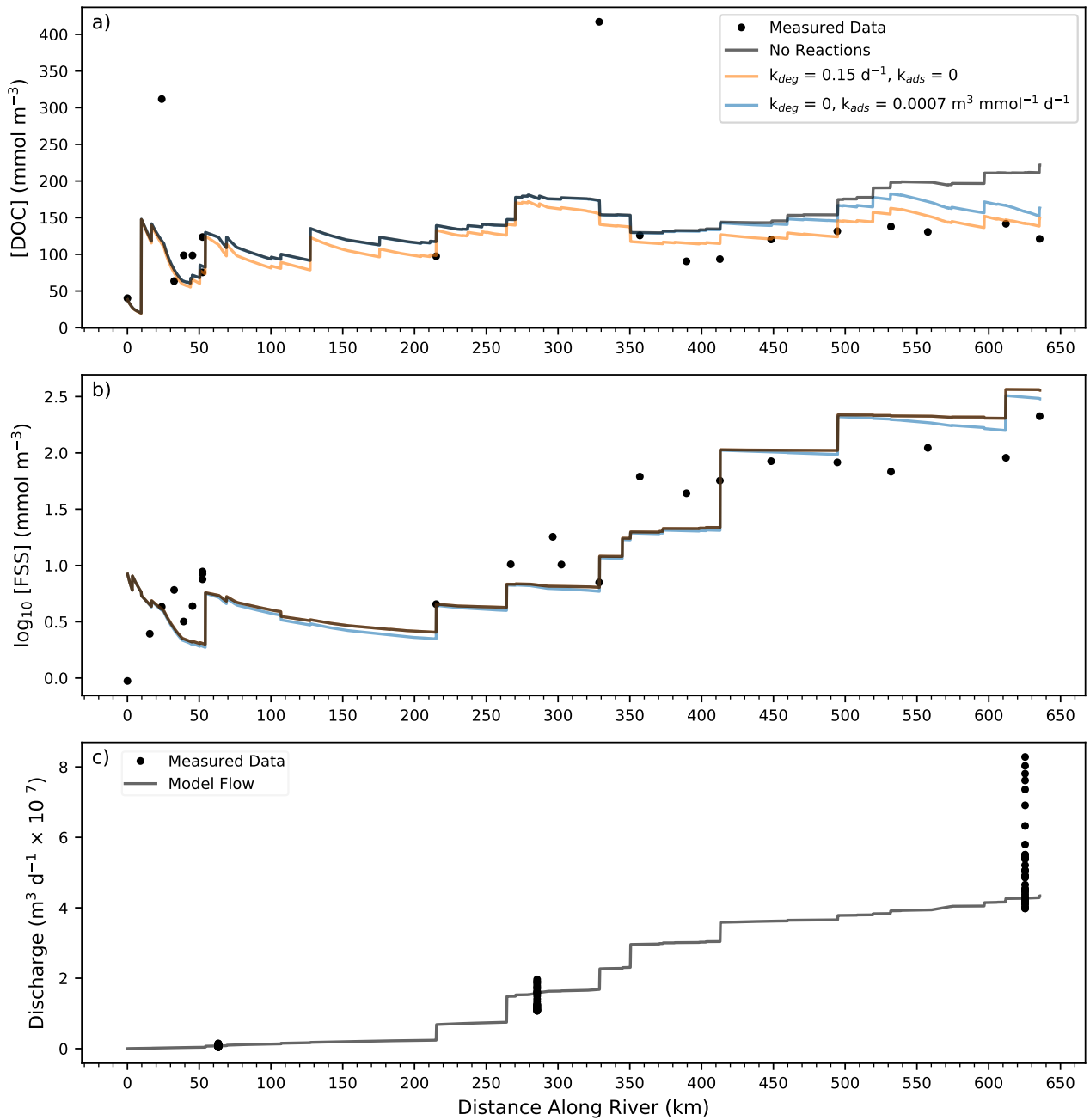


**Figure 7:** Steady state profiles of (a) DOC, (b) FSS and (c) cumulative flow predicted by the model with unmodified input fluxes under three different reaction scenarios (black line = no reactions; orange line = DOC degradation and no adsorption; blue line = adsorption and no DOC degradation). Available measurements (collected across 32 days) are shown as black points.

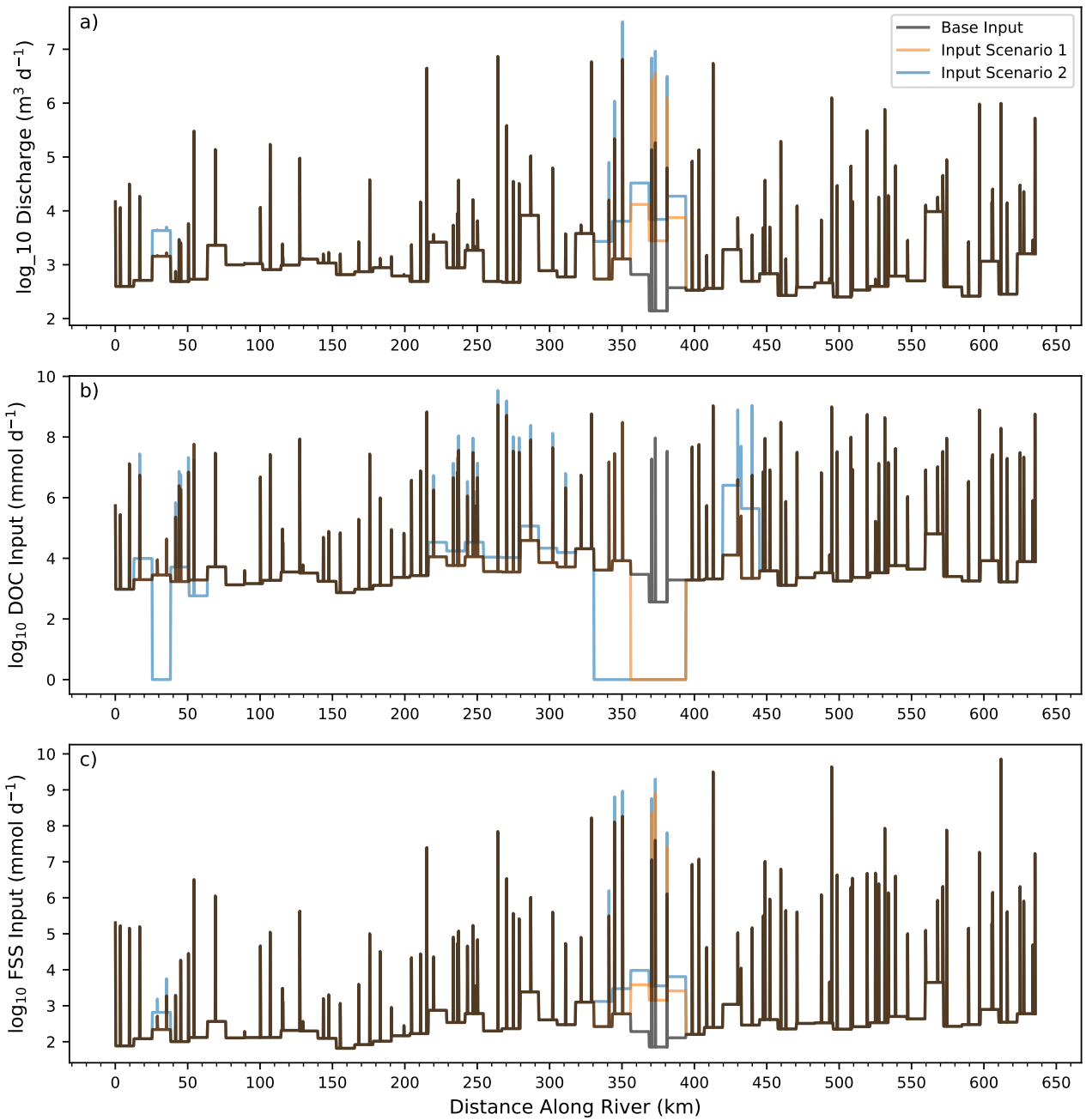


**Figure 8:** Steady state distribution of the lateral input fluxes of (a) water (discharge), (b) DOC and (c) FSS into the main river channel used in the model under three input flux scenarios (black line = no modification (base), orange line = input scenario 1, blue line = input scenario 2). Descriptions of the scenarios can be found in [Section 3.1.3](#). Note that the values in (b) and (c) are equal to discharge times input concentration, so (c) shows differences between the three scenarios despite no direct modification of lateral FSS concentrations.

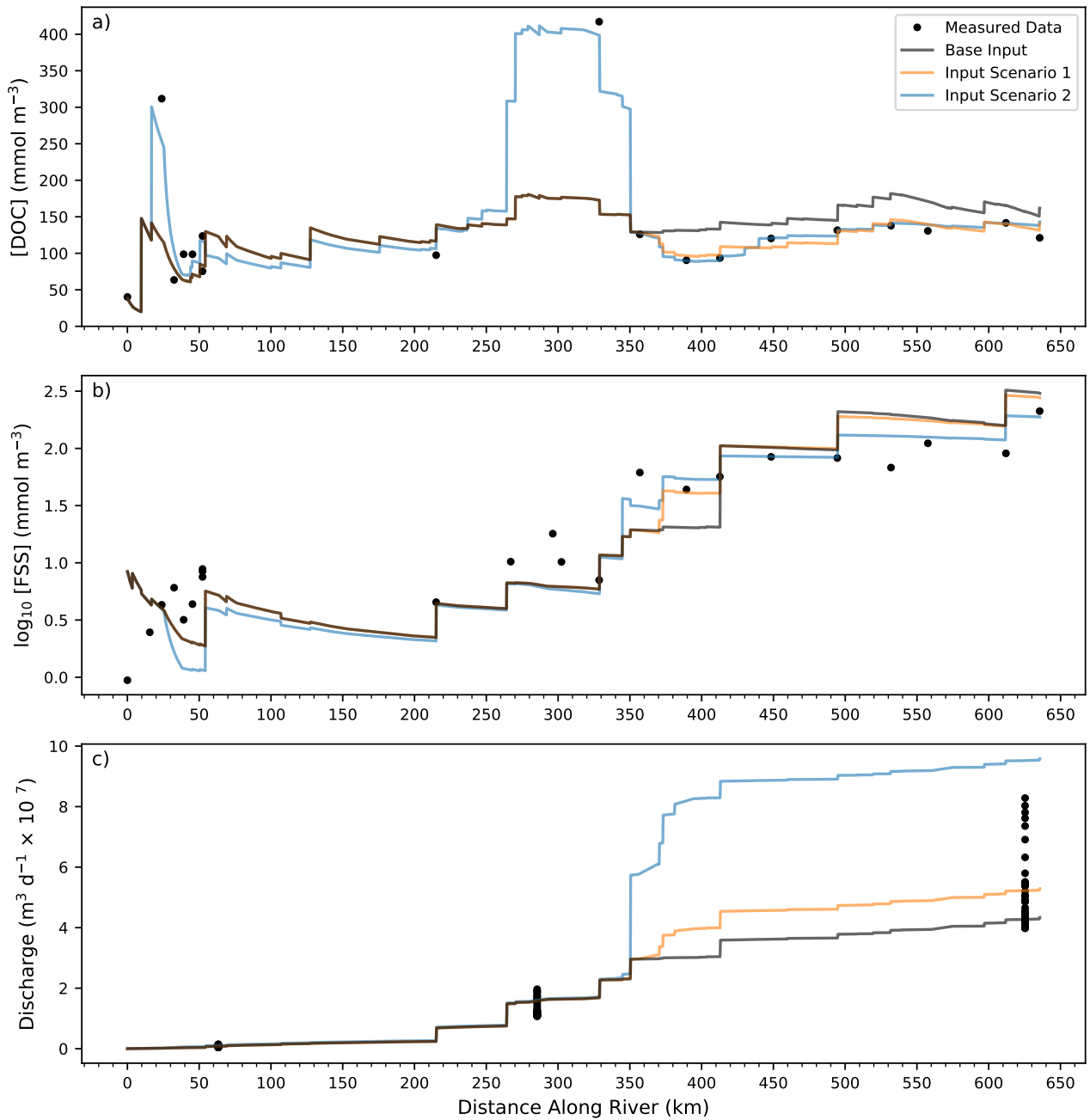


**Figure 9:** Steady state profiles of (a) DOC, (b) FSS and (c) cumulative flow predicted by the model with constant rate constants ( $k_{deg} = 0.003 \text{ d}^{-1}$ ,  $k_{ads} = 0.0007 \text{ m}^3 \text{ mmol}^{-1} \text{ d}^{-1}$ ) under three input flux scenarios (black line = no modification (base), orange line = input scenario 1, blue line = input scenario 2). Descriptions of the scenarios can be found in [Section 3.1.3](#). Available measurements (collected across 32 days) are shown as black points.

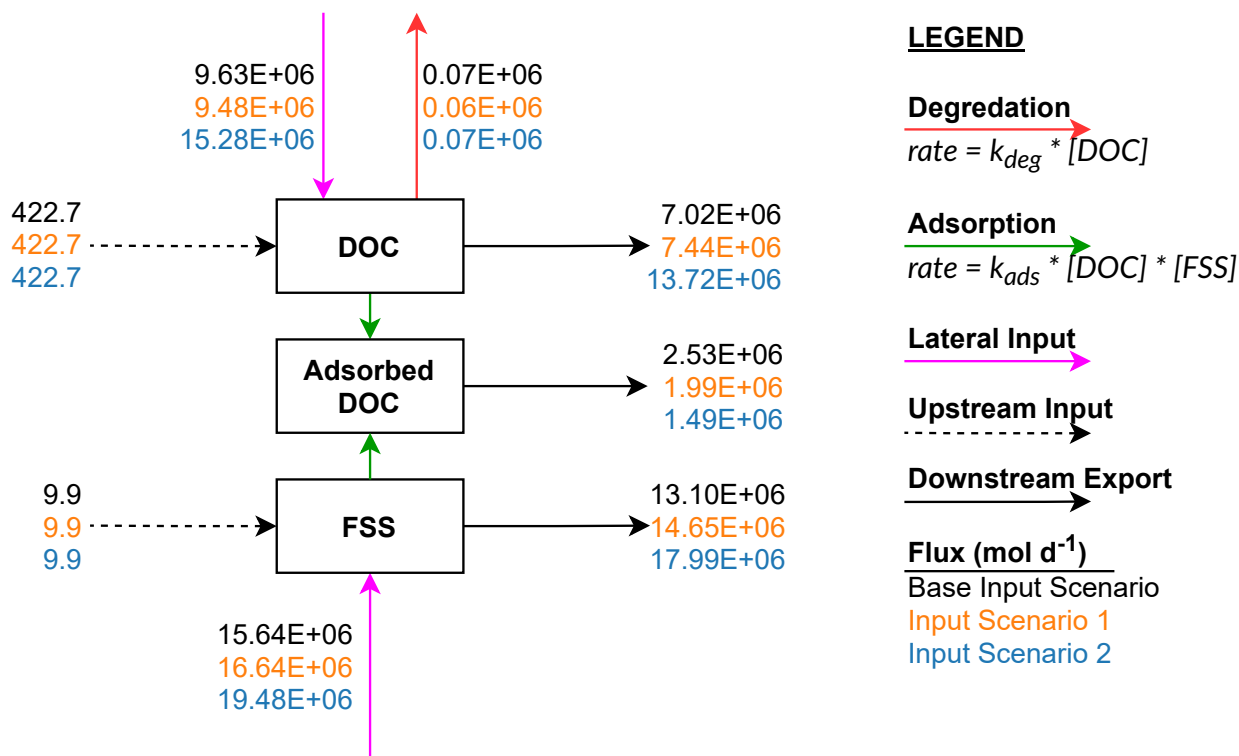


**Figure 10:** A conceptual diagram of the model with fluxes from the three input scenarios. Fluxes were integrated along the entire length of the model domain (635.6 km). DOC fluxes are presented in moles of DOC per day, and FSS fluxes are presented in moles of FSS per day. Note that since no adsorbed DOC removal processes were implemented, the downstream export of adsorbed DOC is equal to the total amount of DOC removed by adsorption in the model domain. The lateral inputs consist of both point (sampled tributaries) and distributed (unsampled zones) sources.

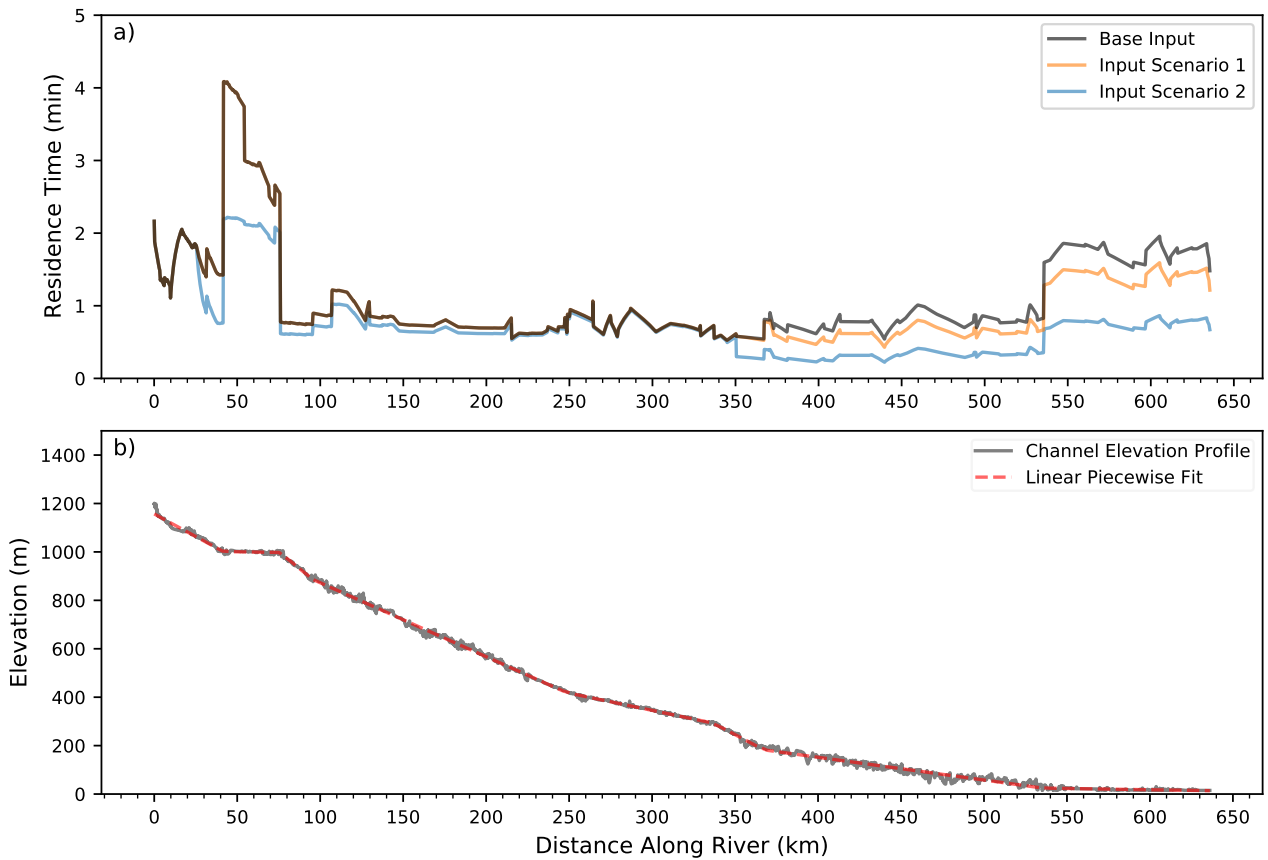


**Figure 11:** (a) Water residence time and (b) channel elevation. Residence times are reported per 127.12 m model cell. The channel elevation profile was approximated with an eight-segment piecewise linear fit. This was necessary due to slight mismatches between the digital elevation model (DEM) and the river line used to sample the DEM, which created positive slopes in the elevation profile.

## 4 Discussion

The model developed in this study was able to predict riverine DOC concentrations surprisingly well considering the roughness of the estimates used to parameterize the model, with the exception of two DOC peaks. Since only steady state solutions are presented, these peaks could be exaggerated by flow variation on a smaller timescale than the model (32 days) or lateral heterogeneities in DOC concentrations in the river.

Based on the modeled scenarios, 70 to 90 percent of DOC input is passed through the model domain unaffected by modeled reactions. Adsorption was the dominant of the two reactions, removing most of the remaining input DOC from the stream, and driven by large TSS inputs in the latter half of the model domain. Additionally, upstream slump affected area did not appear to predict riverine DOC and TSS concentrations, but more work is required to see if this is due to inaccuracies in the classification.

### 4.1 Slump and Burn Scar Classification

Robust training data is essential for accurate predictions from random forest classifiers (Breiman, 2001). In this study, the training data for the slump class was developed from satellite and landscape index trend imagery (Section 2.2.2) by identifying features that could be confidently identified as slumps. Although the classifier classified 94.4% of training points correctly, visual inspection revealed a large number of small slumping features that were impossible to verify. For example, when the classification predicts many small slumping areas along a river channel, it is difficult to assess whether those are thermokarst slumps or just bank erosion as the river slightly changed course over the 19 years that the trend imagery was generated from. The slump class training data would benefit from the addition of a large data set of known slumps from which to sample from, and further analysis should be done to quantify the accuracy of the results. This would potentially improve the correlation between slump affected area and solute concentrations in the river.

The burn class training data was generated by randomly sampling points from the 2000–2019 wildfires data (Section 2.2.2). However, the results of the classification were not straightforward. Some of the known wildfire scars were predicted very accurately, while some were completely classified as neither burn nor slump (Section 3.1.2). Additionally, many large areas were identified as burned that were not contained in the known wildfires data set Section 3.1.2. Some of these discrepancies may be due to differences in the severity of the wildfires, and the fact that the wildfires data set did not contain fires that occurred earlier than the year 2000 which may still have identifiable burn scars. Similar to the slump class, many small burn features were classified across the study basin. It is again difficult to assess the accuracy of these classifications without a quantitative error metric, but one can speculate that these are erroneous classifications since it seems unlikely that so many small wildfires would start without expanding and leaving larger burn scars. Expansion of the wildfires data set to include earlier fires and accounting for fire severity may improve the burn classification.

Overall, the results of the slump and burn classification are dubious because of the lack of a quantitative error metric and the potentially unrealistic dispersal of many small features across the landscape. It was hypothesized that upstream slump affected area would correlate

highly with the DOC or TSS concentrations at sample locations. Analysis revealed that this was not the case (Section 3.1.3), but this could be due to inaccuracies in the classification. Further analysis is required to fully understand and mitigate these inaccuracies.

## 4.2 Flow Predictions

The discharge-area correlation (Figure 3) offered a relatively straightforward way to predict discharges across the study area and was made possible by the existence of five in-situ stream gauges in the study basin. The biggest concern here is that the regression was assumed to extend to areas far below those used to create it, so it is unknown how well the lower area basins conform to this regression. This likely has the largest effect in the beginning sections of the model domain where the river discharge is still low and the effect of high uncertainty on a small input discharge could be noticeable. The regression could be improved by obtaining discharge measurement from basin areas closer to the low end of the prediction range. Since flows appear to play a large role in controlling riverine DOC and TSS concentrations, and are highly variable at a daily timescale (Figure S2), including these variations via daily average flow inputs should be explored and would likely increase the accuracy of model results. A distributed hydrological model that includes precipitation, and soil/atmosphere/groundwater interaction (e.g., Sutanudjaja et al., 2018) would likely provide better flow predictions.

## 4.3 State Variable Concentration Predictions

The average upstream landscape index values were calculated from 19-year mean pixel values since these maps were already calculated for the slump classification. A calculation using values from the sampling period may provide a better correlation. A multi-variable regression including other landscape indices and features (e.g., tasseled cap indices, percent slump affected area, landscape slope) may also improve predictions. Neither of these improvements were explored here due to time constraints. Improvements to the slump classification (Section 4.1) may also change which landscape properties best predict riverine TSS and DOC concentrations.

## 4.4 Model Scenarios — Varying rate constants

The relatively small impact of the modeled reactions on the predicted DOC profile indicates that for most of the model domain, solute transport is the dominant factor controlling DOC concentrations in the river. The effect of degradation is visible throughout the model domain because the degradation rate is dependent only on DOC concentration. Conversely, adsorption has almost no effect until approximately 400 km along the river when TSS concentrations reach a sufficient concentration to drive adsorption to significant levels, which is expected due to the formulation of the adsorption rate law. While adsorption may be the dominant DOC-removing reaction overall, this is only the case because of the high TSS tributaries entering in the latter half of the model domain. The slump classification (Figure 4) reveals that the latter half of the model domain is also where watersheds drain more slump affected area, so it is hypothesised that the high TSS export from thermokarst slumps is driving adsorption to remove additional DOC from solution.

## 4.5 Model Scenarios — Varying Input Fluxes

The input scenarios indicate that the flow of water in the model exerts a high control on DOC concentrations in the channel. Adjusting input flows was the only way to manipulate the profile to fit the observed data because input concentration adjustments did not cause shifts in model results of sufficient magnitude. The high percentages of input DOC that remain as DOC leaving the downstream boundary indicate that advective transport is fast enough that the reactions do not progress very far within the model cells. In the lower reaches of the river, where we see lower velocities, the effect of adsorption becomes more marked, but this appears to be an effect of high FSS concentrations rather than low velocities since there is also a low velocity section in the first 100 km. In this zone FSS concentrations are low and adsorption has little effect, despite the low velocities. Although flow exerts high controls on riverine DOC concentrations, this suggests that reactions, specifically DOC adsorption, are still important processes controlling DOC concentration.

Input scenario 1 represents a reasonable modification of input fluxes since the cumulative model flow in this scenario matches the average measured flow at the downstream boundary. The modifications in this scenario were in a targeted zone, but it is probably not the case that no DOC enters the river in this section and that flows only in this section were underpredicted by a factor of 20. A system wide underprediction of discharge is more likely, and the targeted modifications were able to correct for it.

Input scenario 2 is likely unrealistic, based on the almost double predicted downstream flow in the scenario versus the base input. Additionally, the predicted downstream flow was out of the range of measured downstream flows. However, this is what was necessary to fit the model to the two [DOC] peaks in the measured data. It is important to note that the measured data was collected across 32 days, during which the river flow varied due to precipitation. These variations are averaged out in the input data used in the model to predict DOC and FSS, but the measured data in the graphs reflects a single point in space and time. For example, the measured DOC peak at 350 km was taken on July 24, and one of the in-situ stream gauges (gauge #3 in [Figure 1](#)) happens to be close-by. The hydrograph for this gauge shows that July 24 was part of the rising limb of a precipitation event that almost doubled the discharge of the river in this location ([Figure S2c](#)). Although one would expect a dilution effect with a large input of water, the initial overland flow during a precipitation event can flush sediments and organic materials from the landscape into the channels. The other DOC peak (75 km) was measured on July 4, which shows no such precipitation event (gauge #1 in [Figure 1](#), [Figure S2a](#)). In fact, the sample was taken at the tail end of the falling limb of a precipitation event that happened before the start of the expedition, close to what appears to be the base flow ([Figure S2a](#)). Additionally, the landscape surrounding the section of river where this sample was taken is very boggy and marshy, with small ponds draining intermittently to the channel. It is possible that this sample was collected in the DOC plume of a pond input or simply next to a bank with lots of seepage from the landscape.

## 4.6 Additional Uncertainty and Limitations

The modeling of adsorption as an irreversible process only works when it is limited by the availability of mineral surfaces and far from equilibrium, meaning that net adsorption is positive.

If net adsorption were to be negative (net desorption), that addition of DOC would not be accounted for. This situation could occur from a rapid dilution of DOC in the river from a high flow, low DOC tributary, for example.

The conversion of TSS to FSS was performed to conceptually simplify adsorption during the early stages of model development, since one mole of FSS is consumed for every mole of adsorbed DOC. This conversion could instead be left in the adsorption rate constant. Since it was not, the values used for the conversion bear some discussion. The value for input OC load is debatable since this was measured for overland flow from slumps to channels but applied to measurements containing water that has been in the channel for some time. Additionally, water chemistry and the properties of the suspended sediments and DOM affect the potential for adsorption. Some of this may be captured in the values used in [Section 2.2.5](#), but there is likely still high uncertainty in whether the calculated FSS concentration reflects the number of potential adsorption sites. This may be the source of some of the discrepancy between measured and predicted FSS, but it likely has more to do with the input fluxes. Additionally, some of the over prediction of FSS may be due to the TSS correction applied in [Section 2.2.5](#). The negative TSS values are the result of filter loss during the filtering process, since a clean filter is weighed before and after filtering and drying to calculate the mass of TSS on the filter. This loss can occur in two ways: (i) loss of filter particles due to the suction of the filtering apparatus, and (ii) loss of larger filter pieces when the filter is lifted from the filtering apparatus (i.e., tearing). The first loss mechanism can be accounted for, and for this data was found to be equivalent to approximately 0.22 mg of filter lost per approximately one liter of sample put through a 47 mm glass fiber filter. This value is not nearly large enough to correct the negative values displayed in the data, indicating that the second mechanism is responsible for most of the filter loss. The second filter loss mechanism is difficult to quantify since it can vary widely for each sample due to its dependence on human factors. In the absence of a more accurate way to correct for this and with time constraints in mind, the largest negative TSS value was added to all TSS measurements so that the study could proceed.

The input fluxes for sampled tributaries were implemented as point sources in a one-dimensional model with no dispersion, so they mix completely and instantly with the water in the main channel. This is not the case in reality, as tributaries can have large solute plumes as they mix into the main channel ([Figure S3](#)). So, when samples were taken it is realistic that they may have been taken in a section of river that was not fully mixed, and therefore might not have values representative of the total, mixed channel that the model predicts.

## 4.7 Outlook

This section provides a brief overview of work that could be done to further understand and improve the model presented here. A >1 dimensional transient model that takes into account dispersion and settling processes would likely improve predictions but would also be more difficult to constrain. A transient version of the presented model with daily resolution was developed but there was not enough time to sufficiently process the results, leaving an opportunity for future improvement. Additionally, the DOM pool could be split (recalcitrant vs labile, for example) to provide more insights into the fate of different types of DOM. This would require defining the interactions between these DOM pools, which would be another interesting

continuation of this project.

Overall, sensitivity analyses should be done with respect to many of the parameters used in the model to better understand which parameters should be focused on for estimate improvement. Suggested parameters to analyse are river width, channel roughness coefficient, slope of the regressions used to predict lateral input fluxes, and the surface area and OC loadings used to convert TSS to FSS. As mentioned previously, sensitivity to time dependent events such as precipitation should also be tested.

## 5 Conclusions

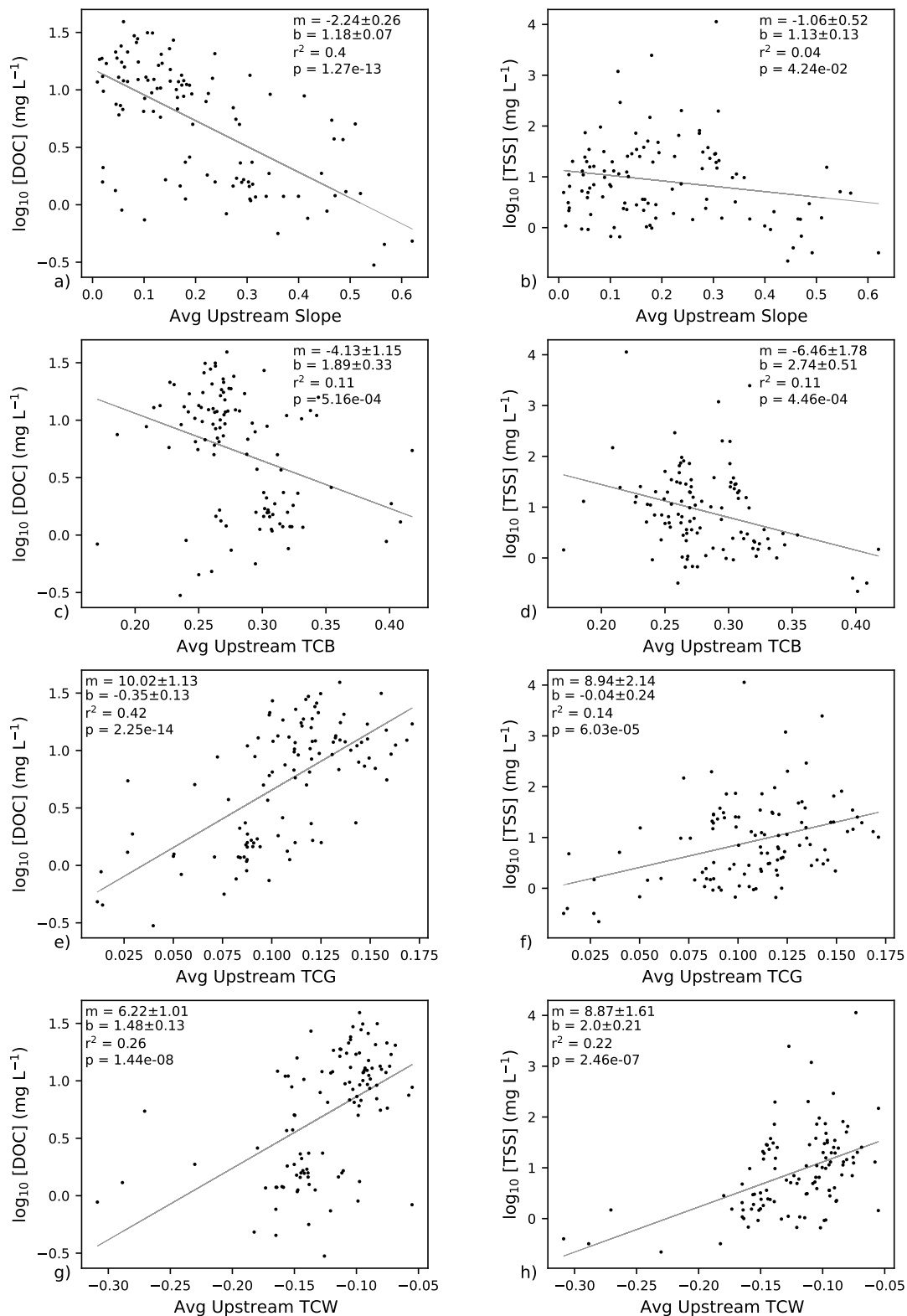
This study suggests that flow of water is the dominant factor controlling riverine DOC and TSS concentrations in the modeled section of the Peel River. Although flow is dominant, DOC mineralization and adsorption to mineral surfaces still play a role, with adsorption driven by large TSS inputs dominating the DOC removal processes. These large TSS inputs maybe due, in part, to increasing slumping activity in tributary watersheds. As a result, 70–90 % of total DOC input to the river was exported from the downstream boundary unaffected by removal processes, and the 10–30 % of input DOC that was removed was predominantly done so via adsorption to mineral surfaces. Additionally, upstream slump affected area did not appear to be a good predictor of riverine DOC or TSS concentrations, but this may be due to inaccuracies in the slump classification.

## References

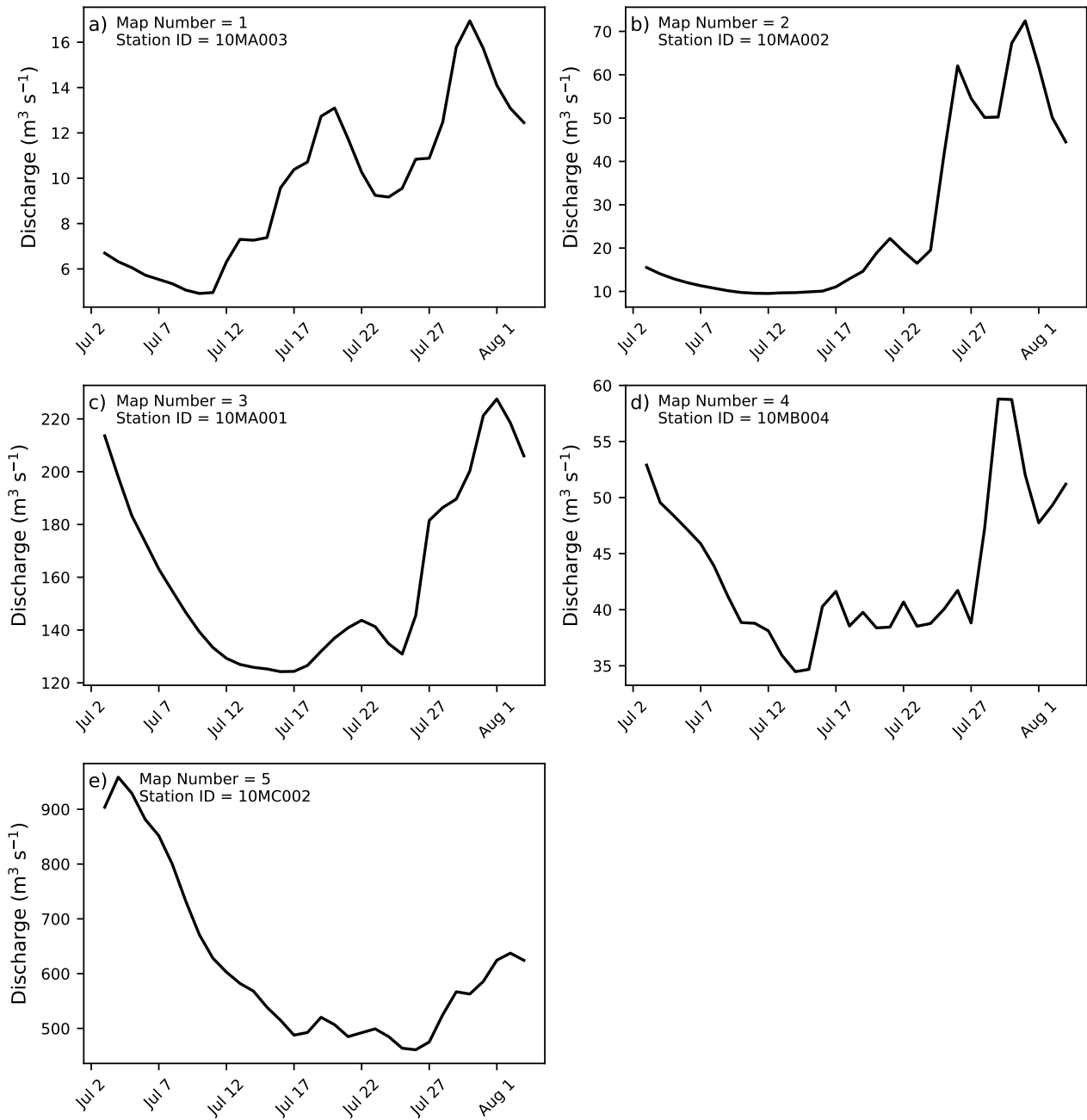
- Arcement, G. J. and Schneider, V. R. (1989). Guide for Selecting Manning’s Roughness Coefficients for Natural Channels and Flood Plains. *Water-supply paper / United States Geological Survey*, 2339.
- Breiman, L. (2001). Random Forests. *Machine Learning*, 45(1):5–32.
- Bröder, L., Keskitalo, K., Zolkos, S., Shakil, S., Tank, S. E., Kokelj, S. V., Tesi, T., van Dongen, B. E., Haghypour, N., Eglinton, T. I., and Vonk, J. E. (2021). Preferential export of permafrost-derived organic matter as retrogressive thaw slumping intensifies. *Environmental Research Letters*.
- Catalán, N., Marcé, R., Kothawala, D. N., and Tranvik, L. J. (2016). Organic carbon decomposition rates controlled by water retention time across inland waters. *Nature Geoscience*, 9(7):501–504.
- Gorelick, N., Hancher, M., Dixon, M., Ilyushchenko, S., Thau, D., and Moore, R. (2017). Google earth engine: Planetary-scale geospatial analysis for everyone. *Remote Sensing of Environment*.
- GRASS Development Team (2017). *Geographic Resources Analysis Support System (GRASS GIS) Software, Version 7.2*. Open Source Geospatial Foundation.

- Kokelj, S. V., Lantz, T. C., Tunnicliffe, J., Segal, R., and Lacelle, D. (2017). Climate-driven thaw of permafrost preserved glacial landscapes, northwestern Canada. *Geology*, 45(4):371–374.
- Mann, P. J., Eglinton, T. I., McIntyre, C. P., Zimov, N., Davydova, A., Vonk, J. E., Holmes, R. M., and Spencer, R. G. (2015). Utilization of ancient permafrost carbon in headwaters of Arctic fluvial networks. *Nature Communications*, 6.
- Manning, R. (1891). On the flow of water in open channels and pipes. *Transactions of the Institution of Civil Engineers of Ireland*, 20:161–207.
- O’Donnell, J. A., Aiken, G. R., Swanson, D. K., Panda, S., Butler, K. D., and Baltensperger, A. P. (2016). Dissolved organic matter composition of Arctic rivers: Linking permafrost and parent material to riverine carbon. *Global Biogeochemical Cycles*, 30(12):1811–1826.
- QGIS Development Team (2021). *QGIS Geographic Information System*. Open Source Geospatial Foundation.
- R Core Team (2017). *R: A Language and Environment for Statistical Computing*. R Foundation for Statistical Computing, Vienna, Austria.
- Schuur, E. A., McGuire, A. D., Schädel, C., Grosse, G., Harden, J. W., Hayes, D. J., Hugelius, G., Koven, C. D., Kuhry, P., Lawrence, D. M., Natali, S. M., Olefeldt, D., Romanovsky, V. E., Schaefer, K., Turetsky, M. R., Treat, C. C., and Vonk, J. E. (2015). Climate change and the permafrost carbon feedback. *Nature*, 520(7546):171–179.
- Soetaert, K. and Meysman, F. (2012). Reactive transport in aquatic ecosystems: Rapid model prototyping in the open source software R. *Environmental Modelling & Software*, 32:49–60.
- Sutanudjaja, E. H., Van Beek, R., Wanders, N., Wada, Y., Bosmans, J. H., Drost, N., Van Der Ent, R. J., De Graaf, I. E., Hoch, J. M., De Jong, K., Karssenber, D., López López, P., Peßenteiner, S., Schmitz, O., Straatsma, M. W., Vannamettee, E., Wisser, D., and Bierkens, M. F. (2018). Pcr-globwb 2: A 5 arcmin global hydrological and water resources model. *Geoscientific Model Development*, 11(6):2429–2453.
- Tarboton, D. G. (1997). A new method for the determination of flow directions and upslope areas in grid digital elevation models. *Water Resources Research*, 33(2):309–319.
- Yamazaki, D., O’Loughlin, F., Trigg, M. A., Miller, Z. F., Pavelsky, T. M., and Bates, P. D. (2014). Development of the Global Width Database for Large Rivers. *Water Resources Research*, 50(4):3467–3480.
- Yang, X., Pavelsky, T. M., Allen, G. H., and Donchyts, G. (2020). RivWidthCloud: An Automated Google Earth Engine Algorithm for River Width Extraction From Remotely Sensed Imagery. *IEEE Geoscience and Remote Sensing Letters*, 17(2):217–221.

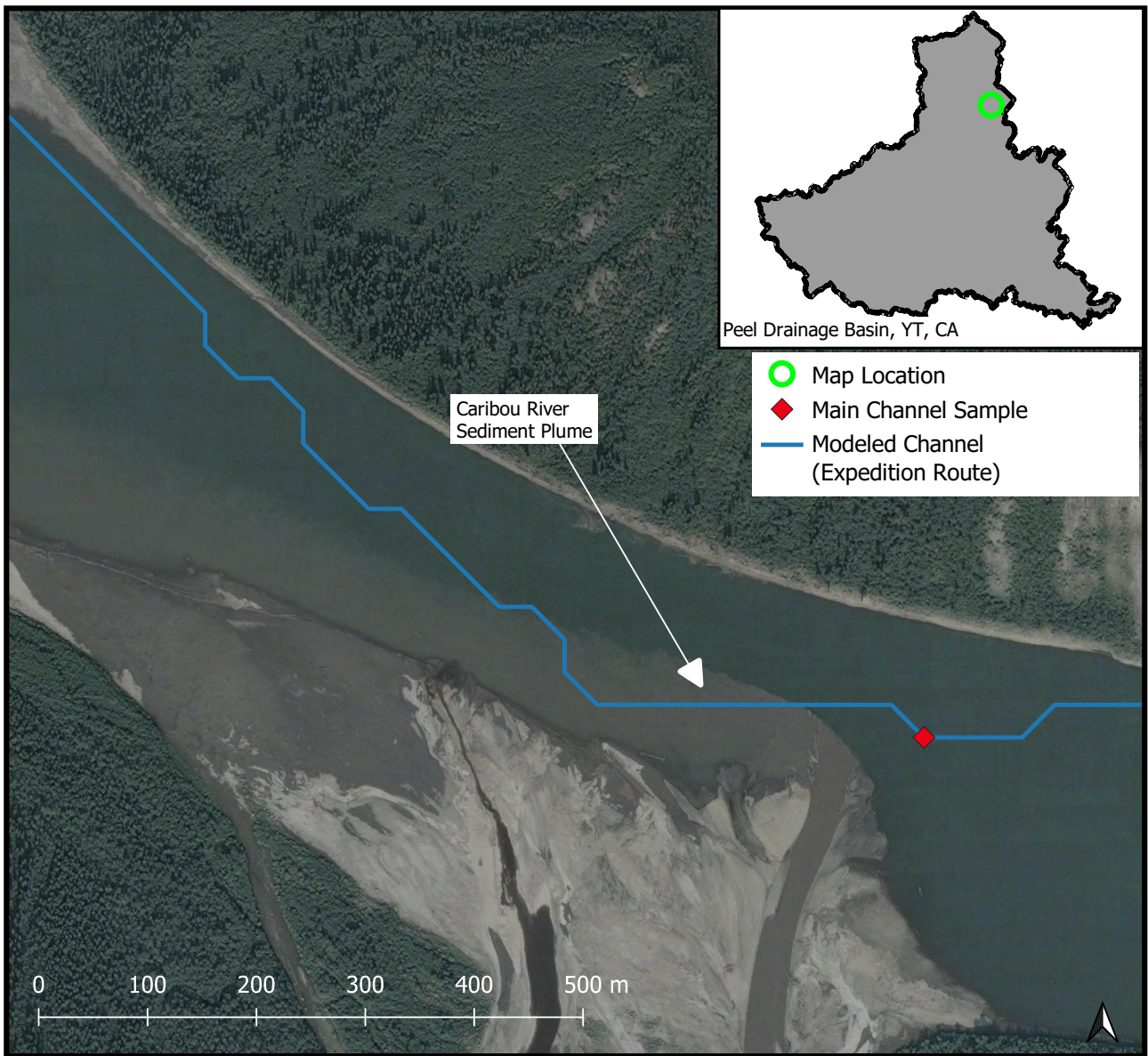
# Supplementary Figures



**Supplementary Figure S1:** DOC (left column) and TSS (right column) measurements tested for correlation against the four landscape properties derived from remote sensing products not presented [Figure 6](#). Best estimates and standard errors of the slope (m) and intercept (b) of the linear regressions are shown.



**Supplementary Figure S2:** Daily discharge hydrographs at the five gauge stations whose map number correspond to the labeled gauges in [Figure 3](#)



**Supplementary Figure S3:** An example of lateral heterogeneity visible from satellite imagery in the Peel River as a result of a turbid tributary (Caribou River) entering at approximately 495 km along the model domain.